materials

MDPI

Article

Graphene Quantum Dots Improved "Caterpillar"-like TiO_2 for Highly Efficient Photocatalytic Hydrogen Production

Jing Ma, Lihua Chu *, Yanjiao Guo, Changxu Sun, Hao Yan, Ze Li and Meicheng Li

State Key Laboratory of Alternate Electrical Power System with Renewable Energy Sources, North China Electric Power University, Beijing 102206, China; JingMa@ncepu.edu.cn (J.M.); ncepugyj@126.com (Y.G.); cxsun@ncepu.edu.cn (C.S.); hyan@ncepu.edu.cn (H.Y.); zli@ncepu.edu.cn (Z.L.); mcli@ncepu.edu.cn (M.L.)
* Correspondence: lhchu@ncepu.edu.cn; Tel.: +86-010-6177-2332

Abstract: Photocatalytic water splitting for hydrogen production via heterojunction provides a convenient approach to solve the world crises of energy supply. Herein, graphene quantum dots modified TiO_2 hybrids (TiO_2-GQDs) with a "caterpillar"-like structure exhibit stronger light absorption in the visible region and an enhanced hydrogen production capacity of about 3.5-fold compared to the pristine TiO_2 caterpillar. These results inferred that the addition of GQDs drastically promotes the interfacial electron transfer from GQDs to TiO_2 through C–O–Ti bonds via the bonding between oxygen vacancy sites in TiO_2 and in-plane oxygen functional groups in GQDs. Using a "caterpillar"-like structure are expected to provide a new platform for the development of highly efficient solar-driven water splitting systems based on nanocomposite photocatalyst.

Keywords: GQDs; TiO_2 caterpillar; photocatalysts; hydrogen production; water-splitting

Citation: Ma, J.; Chu, L.; Guo, Y.; Sun, C.; Yan, H.; Li, Z.; Li, M. Graphene Quantum Dots Improved "Caterpillar" -like TiO_2 for Highly Efficient Photocatalytic Hydrogen Production. *Materials* **2021**, *14*, 5354. https://doi.org/10.3390/ma14185354

Academic Editor: Barbara Pawelec

Received: 23 August 2021
Accepted: 14 September 2021
Published: 16 September 2021

1. Introduction

Global energy inequality, climate change, and consumption of fossil fuels have prompted researchers to turn their attention toward renewable energy [1]. Hydrogen energy is a new green pollution-free energy with many advantages, including high calorific value, easy storage and transportation, etc. [2,3]. Since Fujishima and Honda reported the photoelectrochemical hydrogen evolution process from water in 1972, efficient photoconversion of water to hydrogen has been a long-term goal in the field of photocatalysis [4,5]. Among all the photocatalysts, titanium dioxide (TiO_2) is considered one of the most promising photocatalysts due to its relatively low price, environmental friendliness, superior photocatalytic performance, and long-term stability [6,7]. Wang et al. [8] summarized photocatalytic properties of anatase/bronze TiO_2 in 2020. However, due to the wide band gap energy of TiO_2 (anatase 3.2 eV), its light absorption range is mainly limited to the ultraviolet (UV) region, and the separation efficiency of photogenerated electron-hole pairs is low, which hinders the development of TiO_2 in the field of photocatalysis [9]. In order to improve the photocatalytic performance, heterogeneous catalysts that combine semiconductor quantum dots (QDs) with TiO_2 have been proposed, such as CdS, CdSe, PbS, etc. [10,11].

Among many semiconductor QDs, graphene quantum dots (GQDs) are monolayer or multilayer graphene nanosheets with a transverse size of less than 100 nm [12]; due to its distinctive electronic and optical properties, it has become a research hotspot as photocatalytic nanomaterials [13]. Because of the existence of quantum confinement effect, zero dimensional GQDs have discrete electron energy levels, which is different from nanosheets and nanoribbons [14,15]. In particular, the energy gap of GQDs is adjustable, and it can absorb sunlight of any wavelength by changing its size [16]. Increased studies are trying to apply GQDs to the field of photocatalysis, for example, in 2020, Chen et al. [17] discussed GQDs modified g-C_3N_4 as a photocatalyst and explored its modification mechanism, and

Wei et al. [18] constructed an efficient photocatalyst based on Zn-MOF@GQDs heterostructures. Moreover, it has been proposed that coupling GQDs with TiO_2 has been attempted to improve the charge separation and visible light absorption of the TiO_2 [19–21], but the specific charge transfer mechanism has not been mentioned in most literature.

Herein, TiO_2-GQDs "caterpillar"-like nanoarchitecture hybrids were synthesized and C–O–Ti bond is formed via the connection between the oxygen vacancy in TiO_2 and in-plane oxygen functional groups in GQDs during the ultrasound, thus producing the enhancement of photocatalytic performance in heterostructures. We found that introduction of GQDs on TiO_2 caterpillar was essential to boosting light-driven water splitting for H_2 production, and the working mechanism was elucidated by the schematic diagram of interfacial charge transfer. In work, the inherent defects of TiO_2, such as only absorbing UV light and fast recombination of photogenerated carriers, were improved by compounding with GQDs. These results provide clues for the construction of hybrid nanocatalysts with special morphology of QDs and metal oxides semiconductor, which can be applied in optics, catalysis, and the environment.

2. Materials and Methods

2.1. Chemicals

Concentrated sulfuric acid (98% H_2SO_4) and concentrated nitric acid (68% HNO_3) were obtained from Sinopharm (Shanghai). Sodium hydroxide (NaOH, 96%) was purchased from Aladdin Bio-Chem Technology Co. (Shanghai, China). Titanium dioxide (TiO_2, 99%) for caterpillar, and sodium sulfate (Na_2SO_4) were procured from InnoChem Technology Co., Ltd. (Beijing, China). Acetic acid (CH_3COOH, 99%), $AgNO_3$, tetrabutyl titanate (TBOT), and H_2PtCl_6 were purchased from Sigma-Aldrich Trading Co., Ltd. (Shanghai, China). Nafion solution (perfluorosulfonic acid) was gained from Dupont China Holding Co., LTd. (Shenzhen, China).

2.2. Fabrication of TiO_2-GQDs Caterpillar Hybrids

The GQDs were prepared by chemical oxidation, as reported by Peng et al. [22]. Micrometer-sized pitch-based carbon fibers (0.3 g) were added into a mixture of concentrated H_2SO_4 (60 mL) and HNO_3 (20 mL) with stirring in an oil bath at a temperature of 100 °C for 24 h. After cooling, the mixture was diluted with deionized (DI) water (600 mL), and the pH was adjusted to 8 with NaOH. Finally, the GQDs solution was further dialyzed in a dialysis bag (retained molecular weight: 2000 Da) for 3 days. The TiO_2 caterpillar nanoarchitecture was prepared by the hydrothermal method [23]. TiO_2 nanobelts were first prepared and then placed into the mixed solution with 0.5 mL TBOT, 0.1 g $AgNO_3$, and 40 mL CH_3COOH. After stirring, the solution was transferred to a high pressure reactor which then was heated in a drying oven at 150 °C for 8 h. Subsequently, the product was calcined in a muffle furnace at 450 °C for 1 h to obtain the TiO_2 caterpillar. In order to obtain the TiO_2-GQDs caterpillar hybrids, appropriate amount of TiO_2 caterpillar and GQDs are mixed with ultrasound and stirring for 30 min, finally dried into a powder. All the above steps are conducted in an air atmosphere. The preparation process is shown in Figure 1.

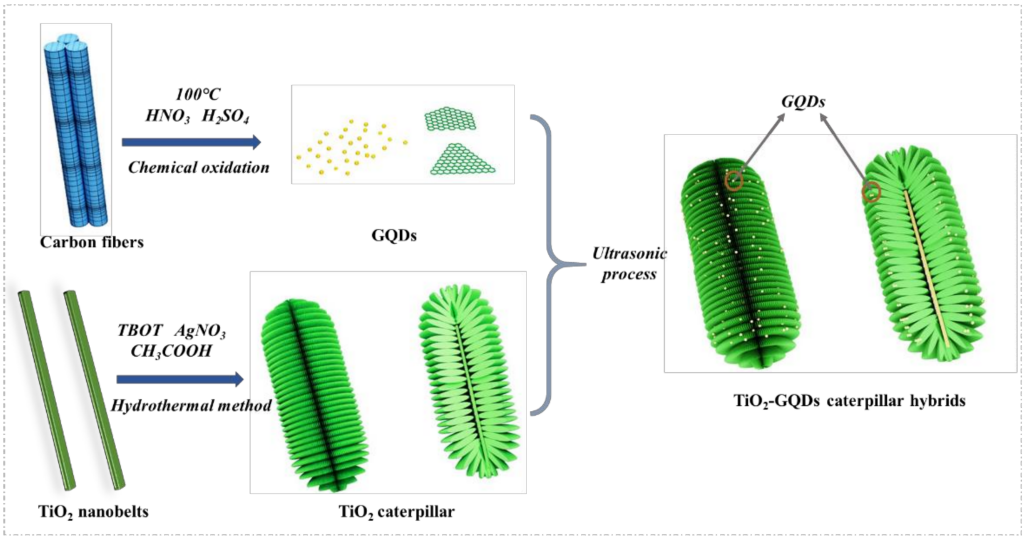

Figure 1. Synthesis of the TiO_2-GQDs caterpillar hybrids nanoarchitecture.

2.3. Characterization and Electrochemical Measurements

The morphology of samples was characterized by scanning electron microscopy (SEM) (SIRION 200, FEI, Hillsboro, OR, USA) and transmission electron microscopy (TEM) using a Tecnai G2 F20 (FEI, Hillsboro, OR, USA). Atomic force microscopy (AFM) (Autoprobe CP-research, Veeco, Plainview, NY, USA) was performed to observe the surface roughness. X-ray diffraction (XRD) analysis (D8 focus, Bruker, Germany) and Raman spectra (Raman-11, Nanophoton, Osaka, Japan) were used to study chemical compositions and structures. X-ray photoelectron spectroscopy (XPS) and valence band XPS (VB XPS) were conducted on ESCALAB 250Xi (Thermo Fisher Scientific, Waltham, MA, USA). Optical absorption spectra were studied by UV-visible diffuse reflectance spectroscopy (DRS) from 200 to 800 nm wavelength (UV-2600, Shimadzu, Kyoto, Japan). Photoluminescence (PL) spectroscopy (FLS980) was used to study the luminescence characteristics of GQDs. Mott–Schottky (M–S) curve measurements were performed on a CHI660E workstation (CH Instruments, Shanghai, China) based on a conventional three-electrode framework with a Pt plate as counter electrode, saturated calomel electrode (SCE) as the reference electrode, and 0.05 M Na_2SO_4 aqueous solution as the electrolyte. Specifically, the working electrodes were prepared by the slurry made of photocatalyst, absolute ethanol, and Nafion solution onto the pretreated fluorine-doped tin oxide (FTO) glass by the dip-coating method, and then dried to form a film electrode.

2.4. Photocatalytic Experiments

The hydrogen production rate under illumination measured the photocatalytic activities of samples. A certain amount of photocatalysts with 5 wt% of Pt (H_2PtCl_6 as a precursor) were dispersed in a top-irradiated photoreactor mixed with DI and methyl alcohol as a sacrificial agent. The reactor was sealed and slowly loaded into a photocatalytic hydrogen production system. Subsequently, the reaction solution was thoroughly degassed before photocatalytic measurement. To adjust the cooling water flow rate, the water temperature is generally set at 5.0 °C. Nitrogen gas was supplied, and a 300 W Xenon light source (66485-300XF-R1, Newport, RI, USA) was turned on. After the experiment started, the system collected and tested H_2 every half hour for about 6 h. The peak area of H_2 obtained from the test results was substituted into the standard curve equation, and the volume of H_2 was calculated. Finally, the hydrogen production amount was calculated by conversion.

3. Results and Discussion

3.1. Morphology Study

The size and morphologies of the pristine TiO_2 caterpillar, GQDs and their hybrids were characterized by SEM, TEM and high resolution TEM (HRTEM). The SEM image of the pristine TiO_2 in Figure 2a reveals a "caterpillar"-like morphology, the 3D bunchy architecture consisted of considerable ultrathin nanosheets. The detailed framework of the TiO_2 caterpillar was further recorded by TEM image (Figure 2b). It is observed that the nanosheets are as thin as the nanometer level, while the length of caterpillar nanoarchitecture is ~10 μm, and the radius is ~0.72 μm. Figure 2c shows the HRTEM image of the pristine TiO_2 and its corresponding selected area electron diffraction (SAED) pattern. Interplanar spacing of around 3.5 Å assigned to the (101) plane of TiO_2 crystal [24] and the SAED pattern shows its polycrystalline properties. GQDs with average size ∼5 nm in diameter and a lattice spacing of 0.32 nm corresponding to the (002) plane are displayed in Figure 2d. As Figure 2e reveals, the GQDs attach to the surface and inside of the TiO_2 nanosheets in the caterpillar nanoarchitecture, which was not destroyed after the ultrasonic treatment. To further confirm the coupling of the GQDs with TiO_2, Figure 2f indicates the HRTEM lattice image of the TiO_2-GQDs hybrid sample, where the lattices of both TiO_2 and GQDs are well-defined, revealing the strong attachment of the GQDs over the TiO_2 surface. The average diameter of GQDs shown with dotted circles is about ~5 nm, which is consistent with the result of Figure 2d. The inset in Figure 2f shows the corresponding fast Fourier transform (FFT) pattern of GQDs confirming the sp^2 hybridized, hexagonal graphitic structure [25]. As mentioned above, "caterpillar"-like morphology refers to substantial nanosheets attached to the nanobelt existing in the center of 3D bunchy architecture, which possesses a large surface area and may provide more exposed active sites and decrease the transmission distance of photo-excited electron-hole pairs.

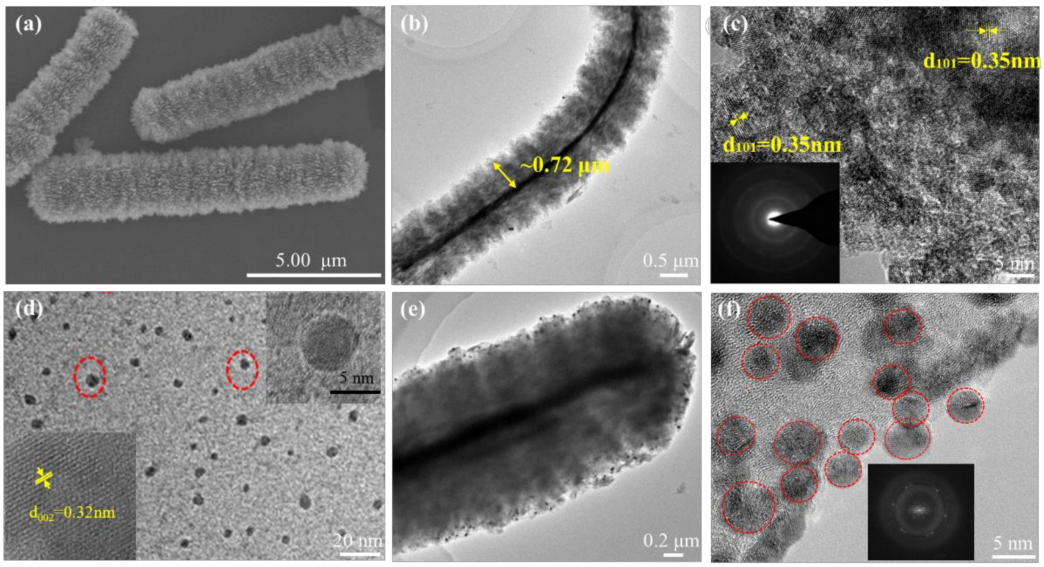

Figure 2. (**a**) SEM, (**b**) TEM and (**c**) HRTEM images of pristine TiO_2. (**d**) TEM image of GQDs showing an average size of ∼5 nm. The inset shows the HRTEM lattice image. (**e**) TEM and (**f**) HRTEM images of TiO_2-GQDs caterpillar hybrid. The inset in image in (**f**) is the FFT pattern of GQDs.

3.2. Characterization of GQDs

To further study the properties of the GQDs, AFM analysis has been conducted. The AFM image of GQDs and the particle size distribution are shown in Figure 3a,b. The bright spots indicate the existence of nanometer GQDs. Line profile measurement for GQDs is obtained by Gwyddion software tool [26], indicating that the GQDs sample has an average height of 0.8–1.2 nm, which corresponds to 2–3 graphene layers. Furthermore, the optical properties of GQDs were studied by the PL technology with different excitation

wavelengths. As shown in Figure 3c, with the excitation wavelength increasing from 350 to 450 nm, the PL peaks red-shift from 470 to 530 nm and cause a decrease in the PL peak intensity elucidating the excitation-dependent PL behavior of GQDs, which reveals a Stokes shift and corresponds to the confinement effect [27]. The full-width at half-maximum (FWHM) of PL peaks is about 100 nm, which is a typical value of carbon-based quantum dots [26]. Figure 3d shows that GQDs solution emits bright blue fluorescence under 365 nm UV light, which is caused by the down conversion characteristics [28]. These PL results confirm that the quantum dots have completely localized electronic states and unique optical properties, which will give full play to their advantages when coupled with TiO_2.

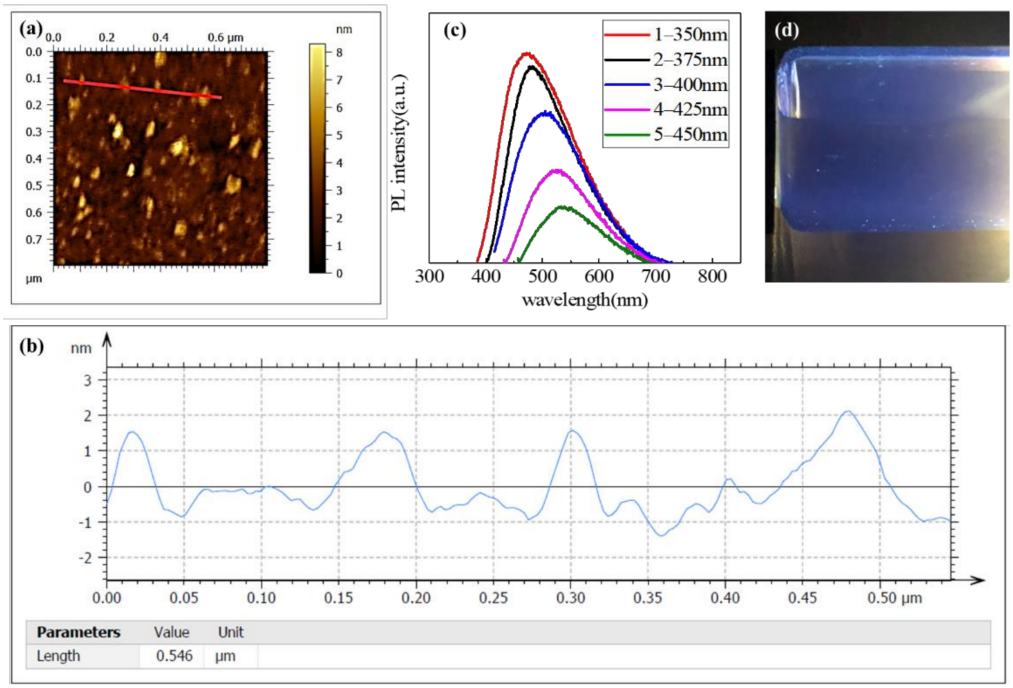

Figure 3. (**a**) AFM image and (**b**) line profile measurement for GQDs. (**c**) PL spectrum of GQDs with different excitation wavelengths, (**d**) luminescence characteristics of the GQDs solution under UV light (365 nm).

3.3. XRD and Raman Spectroscopy Studies

The prepared pristine TiO_2 caterpillar and hybrids of GQDs and TiO_2 show excellent crystallinity, as evidenced by XRD results (Figure 4a). In the pristine TiO_2, the intense peaks at 25.31°, 37.79°, and 48.04° correspond to the anatase phase (101), (004), and (200) planes of TiO_2 (JCPDS Card no. 21-1272), respectively. In addition, it can be seen that there is a characteristic peak of rutile TiO_2 (JCPDS Card no. 21-1276), but the peak intensity is weak. In the TiO_2-GQDs caterpillar hybrid sample, the obvious peak at 26.3° corresponds to the (002) plane of sp^2 carbon in GQDs. No other diffraction peaks related to GQDs were observed in the XRD pattern due to the low concentration of GQDs in the hybrid. As compared to pristine TiO_2 caterpillar, the decrease in crystallinity of hybrid may be due to the ultrasonic treatment that causes defects or disorder. Raman spectroscopy can be used to characterize semiconductor nanostructures and graphite based materials. Using Raman spectroscopy, the changes in the crystallinity/disorder, defects, and internal stress of the samples can be observed. The Raman spectra collected from the GQDs, TiO_2 caterpillar, and TiO_2-GQDs caterpillar hybrids in the region of 100–1900 cm^{-1} are shown in Figure 4b. Both the TiO_2 and TiO_2-GQDs caterpillar hybrid samples show the characteristic Raman bands of anatase TiO_2, such as three E_g, two B_{1g}, and one A_{1g} modes [29], indicating that ultrasonic treatment will not change the phase of TiO_2. The strongest $E_g(1)$ mode that corresponds to the symmetric lattice angular vibration of the O–Ti–O bond is the characteristic peak of anatase TiO_2, which is consistent with the literature [30]. It can be seen that the Raman

$E_g(1)$ centers of TiO_2 and TiO_2-GQDs hybrid are 145.4 cm^{-1} and 147 cm^{-1}, respectively, and the peak shifts by 1.6 cm^{-1}, indicating the strong interaction between the GQDs and TiO_2 in TiO_2-GQDs hybrid. In the case of TiO_2-GQDs caterpillar hybrid, the broadening in Raman line shape is possible due to the lattice strain caused by covalent bond, such as C–O–Ti. The D and G peaks observed on Raman spectra are typical to graphene-based materials. The first Raman peak in GQDs, the G band is an in-plane vibration of C=C sp^2 hybridized carbon atoms, which belongs to the E_{2g} irreducible representation. In addition to the identified G peak, the defect-induced D peak which originates from the "unorganized" carbon associated with the defects or edges of graphene [24,31]. The type of edge configuration of GQDs can be determined by the intensity of D band. The D band is prominent for the armchair edges but absent for the zig-zag edges of GQDs. As a result, the D band of TiO_2-GQDs is inconspicuous, such that the GQDs edges are zig-zag in the hybrids. In order to estimate the relative contributions of the in-plane and the edge states, the Raman intensity ratios of the D band to G band (ID/IG) [32] in GQDs and TiO_2-GQDs hybrid were calculated with the ratios of 1.28 and 1.15, respectively. The results show that the ID/IG ratios of the samples change only slightly, indicating that the GQDs have a uniform edge configuration. It shows that despite the TiO_2-GQDs hybrid being formed, the GQDs edge type did not change, which implies that the change mainly occurs in the in-plane oxygenated functional (epoxy) groups of GQDs. The epoxy groups in the edge and in-plane are redistributed and provide the in-plane epoxy C–O in the process of ultrasonic treatment, which is directly related to the bonding of TiO_2 caterpillar with the GQDs through the connection of basal plane C–O to the Ti in TiO_2.

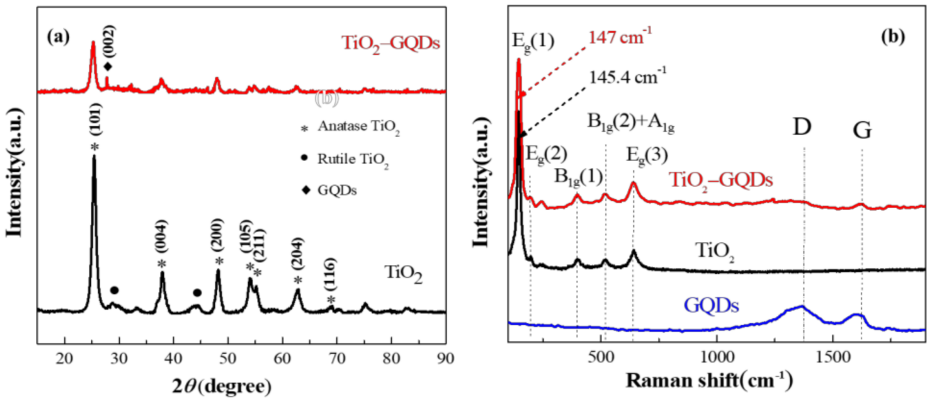

Figure 4. (**a**) XRD results of pristine TiO_2 and TiO_2-GQDs caterpillar hybrid. The symbols of "*", "•", and "♦" correspond to the anatase TiO_2, rutile TiO_2, and GQDs, respectively. (**b**) Characteristic Raman spectra of pristine TiO_2 caterpillar, GQDs and TiO_2-GQDs caterpillar hybrid. The Raman of TiO_2 and GQDs are marked with standard symbols. To ensure clarity, the curve moves vertically.

3.4. XPS Studies

In order to further study the covalent bond in the hybrid, XPS was performed on the TiO_2 caterpillar, GQDs, and TiO_2-GQDs hybrids. Figure 5a,b shows the C1s spectra of GQDs and TiO_2-GQDs caterpillar hybrid, which is fitted by four typical Gaussian peaks, and the centers are near 284.5 eV (P1), 286.1 eV (P2), 287.5 eV (P3), and 290.1 eV (P4). The peak located at the P1 corresponds to the C=C, which originated from the honeycomb lattice structure of sp^2 hybridized carbon atoms. The peaks of P2, P3 and P4 are attributed to oxygen related functional groups in GQDs, respectively, which are C–O (ether) (P2), C=O (P3), and COOH (P4) [33–35]. It can be seen from the Figure 5b that the C–O and COOH peaks in the hybrid are reduced, which may be due to their poor stability. Therefore, unstable related functional groups can be transformed into in-plane epoxy groups to promote the formation of C–O–Ti bonds. The difference is that the edge carbon atoms bonded to C=O are highly stable and do not change during the formation of hybrid [36,37]. In addition, in Figure 5b, no functional groups related to Ti–C bond was

found in the C1s spectrum of the TiO_2-GQDs hybrid, which indicates that Ti and C are bonded by oxygen atom to form C–O–Ti covalent bonds [38]. The changes of surface states in TiO_2-GQDs caterpillar hybrid samples are evaluated by the O1s XPS spectra, as Figure 5c,d show. The TiO_2 caterpillar spectrum is fitted with two Gaussian peaks at binding energies of 529.7 and 531.2 eV, which are attributed to the lattice oxygen (Ti–O) [39,40] and surface hydroxyl group (Ti–OH) caused by the oxygen vacancies on the surface, respectively, suggesting the existence of adsorbed hydroxyl groups or water molecule [41]. In contrast, the O1s spectrum of TiO_2-GQDs hybrids shows a difference. Three Gaussian peaks are fitted, which are located at 529.6 eV, 531.0 eV, and 535.5 eV, according to the XPS spectrum. Similarly, the peak centered at 529.6 eV is related to the oxygen in the crystal (Ti–O–Ti bond) [34]. In the literature [35,37,42], the XPS peaks in the range of 530.0–532.1 eV is usually attributed to the C–O–Ti bond; thus, it is considered that the strong peak at 531.0 eV comes from the C–O–Ti bond [38], which originates from the oxygen vacancy sites in TiO_2 and in-plane oxygen functional (epoxy) groups in GQDs. Additionally, a new contribution with a maximum of 535.5 eV appeared, which is called hydroxyl functional group (C–OH) [36] when introducing GQDs. The Ti2p XPS spectra of the TiO_2 caterpillar and TiO_2-GQDs hybrid were also collected. The Ti2p consists of Ti^{4+} $2p_{3/2}$ (458.7 eV) and Ti^{4+} $2p_{1/2}$ (464.3 eV) spin-orbital as shown in Figure 5e, where it is typically referring to the characteristic of Ti^{4+}-O bonds in TiO_2 [43]. However, in the case of TiO_2-GQDs caterpillar hybrids, along with $Ti2p_{3/2}$ (458.4 eV) and $Ti2p_{1/2}$ (464.1 eV) binding energies peaks, two new binding energy peaks at 457.7 eV and 463.4 eV are observed associated with Ti^{3+} valence states. The binding energy different (Δ) between (Ti^{4+} $2p_{1/2}$–Ti^{4+} $2p_{3/2}$) and (Ti^{3+} $2p_{1/2}$–Ti^{3+} $2p_{3/2}$) is 5.7 eV, which is similar to the report by previous study [44]. This unambiguously demonstrates the formation of Ti^{3+} valence states caused by oxygen vacancy during the process of ultrasound. Furthermore, the hybrids are slightly shifted towards lower binding energy compared with those in pure TiO_2 caterpillar, suggesting that the chemical environment of Ti in the TiO_2-GQDs has been changed due to the strong interaction of C–O–Ti bond between the TiO_2 and GQDs. Therefore, the above results based on the XPS spectra indicate the existence of Ti^{3+}, oxygen vacancies and C–O–Ti bond when coupled GQDs with TiO_2 caterpillar, which may help to reduce the band gap of TiO_2 and greatly promote the separation of photogenerated electrons and holes.

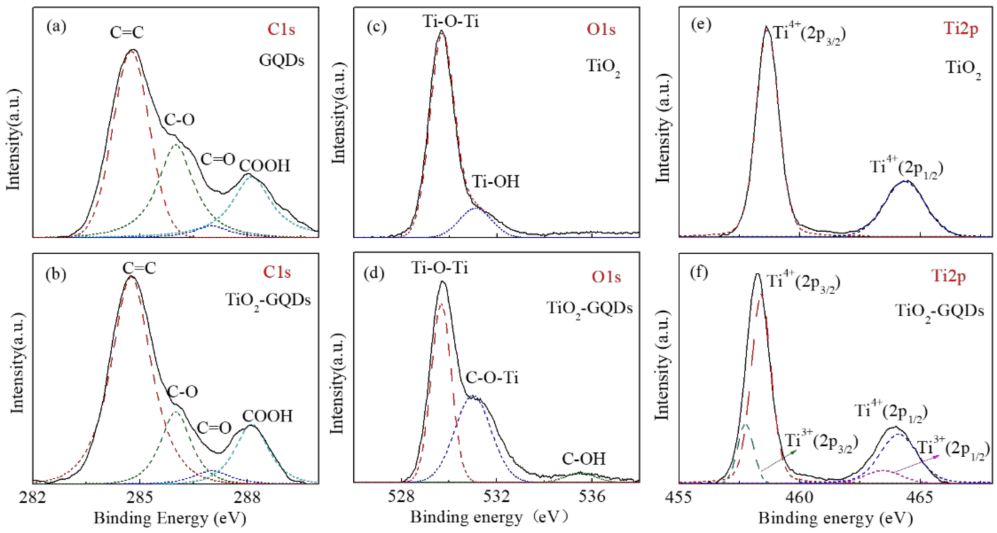

Figure 5. High-resolution XPS spectra of samples: (**a**,**b**) C1s spectra for GQDs and TiO_2-GQDs caterpillar hybrid, (**c**,**d**) O1s, and (**e**,**f**) Ti2p for TiO_2 caterpillar and TiO_2-GQDs caterpillar hybrid.

3.5. UV-Visible Absorption and Band Structure Studies

As photocatalysts, the light absorption performance of samples is critical. The UV-vis absorption spectrum of GQDs, TiO_2 caterpillar, and their hybrids samples are depicted in Figure 6a. In the spectrum of prepared GQDs, intense absorption in the UV region with the tail of the absorption band extending to the visible range and a weak absorption peak as a shoulder centered around 350 nm are associated with n→ß* transition of C=O [27,45]. Therefore, this absorption spectrum is further evidence for the fabrication of GQDs. We can see that pristine TiO_2 caterpillar nanoarchitecture can absorb most of the light in the UV region, and the absorption edge wavelength is around 420 nm, while the absorption edge of TiO_2-GQDs hybrid sample is visibly red-shifted due to the synergistic effect between TiO_2 and GQDs, showing stronger absorption in the visible region. The expansion of light absorption range is beneficial to visible light photocatalysis. This indicates that the incorporation of GQDs reduces the band gap relative to pure TiO_2 caterpillar. The band gap narrowing and extended absorption should be attributed to the hybrid formation through the chemical bonding between TiO_2 and GQDs, i.e., the formation of C–O–Ti covalent bonds, similar to carbon-doped TiO_2 composites. Under light irradiation, this C–O–Ti bond will facilitate the efficient interfacial charge transfer from GQDs to the TiO_2 caterpillar, thus prolonging the absorption of the hybrid in the visible region, resulting in the improved photocatalytic performance of the TiO_2-GQDs. Furthermore, the optical bandgap energy (E_g) of the samples could be estimated by the transformational Tauc's plot obtained from the Kubellka–Munk function [46]:

$$(\alpha h\nu) = A\left(h\nu - E_g\right)^{n/2}, \tag{1}$$

where α is the absorption coefficient, h is Planck's constant, A is a constant, ν is the light frequency, and n = 1 and 4 for direct and indirect band gap materials, respectively. The optical transitions of TiO_2 are indirect and the value of n is thus 4 [47], while n = 1 for GQDs [18]. Figure 6b shows the plot of $(\alpha h\nu)^{1/2}$ versus $h\nu$ of TiO_2 caterpillar and TiO_2-GQDs hybrid. Using the Tauc plot, we estimated the E_g of TiO_2 and TiO_2-GQDs caterpillar nanostructure to be around 2.95 and 2.72 eV, respectively. This is further proof that when TiO_2 caterpillar is combined with GQDs, its band gap reduces, and thus the response range in visible light is improved. Similarly, Figure 6c shows the E_g of GQDs is around 2.35 eV.

To gain insights into the intrinsic properties and effects of GQDs on the band structure of the TiO_2, the flat band potentials (V_{fb}) of GQDs, TiO_2 caterpillar and TiO_2-GQDs caterpillar hybrid were measured by M–S plots, which can be estimated from the plots based on Equation (2) [48]:

$$\frac{1}{C^2} = \left(\frac{2}{\varepsilon_r \varepsilon_0 e N_d A^2}\right)\left[\left(V - V_{fb}\right) - \frac{kT}{e}\right], \tag{2}$$

where C is the specific capacity and V_{fb} is the flat band potential. It can be seen that the reciprocal of the square of capacity ($1/C^2$) has a linear relationship with the applied potential (V), and take them as Y-axis and X-axis, respectively, as shown in Figure 6d–f, the intercept of the line on the X-axis is the V_{fb}. Furthermore, the V_{fb} and the positive or negative slope of the line can be used to estimate the position of the conduction band (CB) or valence band (VB), respectively. For example, the negative slope of the tangent line in Figure 6d indicates the highest potential of the VB can be extremely close to its V_{fb}. As a result, the V_{fb} of TiO_2 caterpillar was calculated to be 2.02 V vs. SCE (2.26 V vs. standard hydrogen electrode (NHE)). In Figure 6e, the tangent line with a positive slope indicates the lowest potential of CB could be estimated from its V_{fb} accordingly. Therefore, the CB bottoms of the GQDs were confirmed to be −1.18 V vs. SCE (−0.94 V vs. NHE). Furthermore, combined with E_g of GQDs in Figure 6c, the VB values of GQDs were calculated to be 1.41 V vs. NHE. An inverted V-shape is shown in Figure 6f, indicating that a heterojunction forms at the interface between TiO_2 caterpillar and GQDs with distinct electronic behavior. Thus, the CB and VB in the TiO_2-GQDs caterpillar hybrids were determined to be −0.87 V vs. SCE (−0.63 V vs. NHE) and 1.86 V vs. SCE (2.10 V vs. NHE),

respectively [49,50]. In order to better elucidate the energy band structure of photocatalysts, the exact VB positions for TiO_2 caterpillar and TiO_2-GQDs caterpillar hybrid were also verified by VB XPS measurement, which can give information related to the total density of states (DOS) of the VB [48,51]. As shown in Figure 6g,h, the maximum VB energies of TiO_2 and TiO_2-GQDs caterpillar hybrid were estimated to be at 2.27 eV and 2.09 eV, respectively, indicating the alteration of the electronic structure after introducing GQDs. Meanwhile, combined with the E_g in Figure 6b, the minimum CB energies may be obtained to be at about −0.68 eV for TiO_2 caterpillar and −0.63 eV for TiO_2-GQDs caterpillar hybrid. Both of the results conform well to the V_{fb} values estimated in Figure 6d,f. Therefore, according to the analysis of the energy band positions of the above different samples, the band structures of TiO_2 caterpillar and TiO_2-GQDs caterpillar hybrid compared to the potentials for water reduction and oxidation were well resolved, as illustrated in Figure 6i [52,53]. It was concluded that GQDs, TiO_2, and TiO_2-GQDs all have appropriate energy level positions, which meet the thermodynamic condition for photocatalytic splitting of water toward hydrogen evolution. Compared to pristine TiO_2, a more positive CB of TiO_2-GQDs caterpillar hybrid may reduce thermionic emission induced by high potential barrier height of the photocatalyst-Pt contact [49].

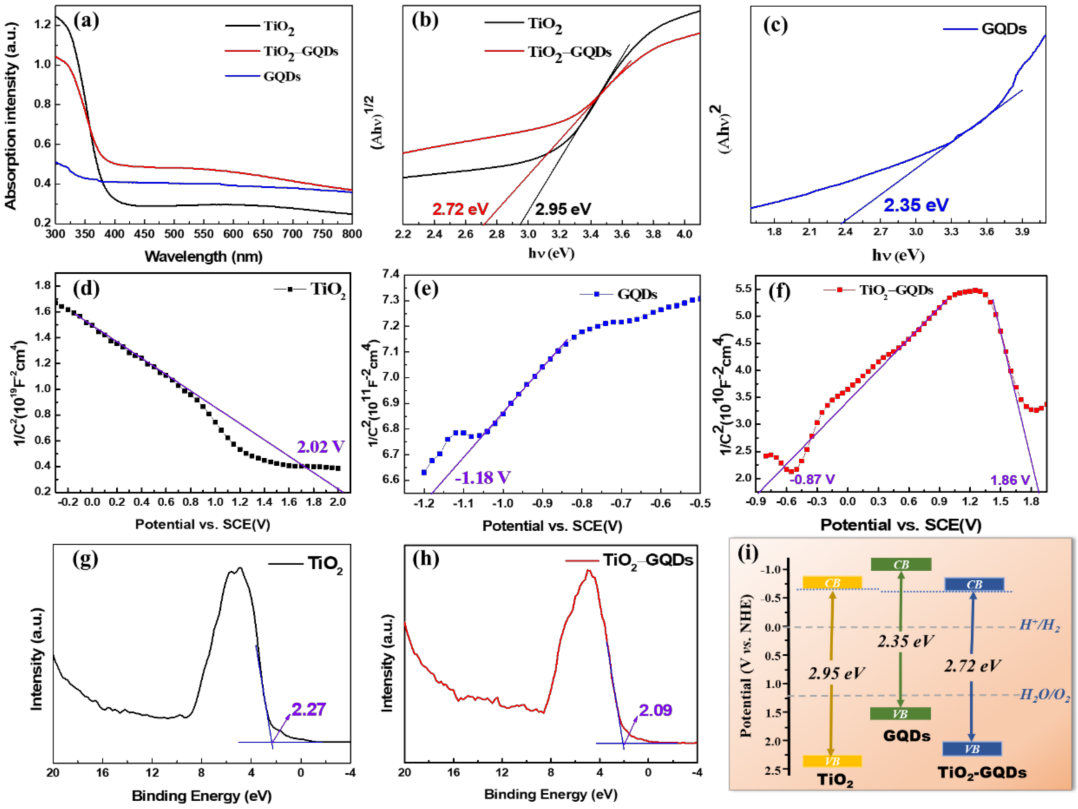

Figure 6. (**a**) UV-vis DRS. (**b**) The plots of (Ahν) $^{1/2}$ versus hν of TiO_2 caterpillar and TiO_2-GQDs hybrid samples and (**c**) the plots of (Ahν) ^{2} versus hν of GQDs. (**d**) M–S curves collected on TiO_2 caterpillar, (**e**) GQDs and (**f**) TiO_2-GQDs caterpillar hybrid. (**g**) VB XPS spectra of TiO_2 caterpillar and (**h**) TiO_2-GQDs hybrid. (**i**) Band structure diagram of GQDs, TiO_2 caterpillar and TiO_2-GQDs caterpillar hybrid.

3.6. Photocatalytic Properties Studies

In order to study the photocatalytic performance of TiO_2 caterpillar after introducing GQDs, the photocatalytic water reduction for hydrogen production under simulated solar light irradiation using TiO_2 caterpillar, GQDs, and TiO_2-GQDs hybrid were further investigated. Since Pt is a traditional and efficient co-catalyst, H_2PtCl_6 is used as a precursor to reduce the overpotential required for water decomposition to hydrogen production [54]. From Figure 7a, it can be seen that hydrogen production of all samples increases with the

extension of irradiation time. After 360 min of light irradiation, total hydrogen evolution over pure TiO_2 caterpillar and GQDs reached 30 and 70 μmol, respectively. In contrast, the photocatalytic H_2 evolution activity of TiO_2-GQDs caterpillar hybrid was significantly enhanced, which reached the maximum H_2 production of 110 μmol. Additionally, as Figure 7b shows, the pure TiO_2 caterpillar exhibited a relatively low hydrogen production rate (5.2 μmol/h); this may be because the absorption range of TiO_2 is limited to UV light and a small part of visible light, and the photogenerated charge carriers recombine quickly. After coupling with GQDs, the H_2 generation rate of hybrid was the highest (18.3 μmol/h), which is about 3.5 times the H_2 production rate of pure TiO_2 caterpillar. Moreover, the H_2 evolution rate of pure caterpillar and hybrid are higher than that of P25 (2.3 μmol/h) and CQDs/P25 (9.1 μmol/h) reported by Yu et al. [55] and are also higher than that of pure TiO_2 (0.3 μmol/h) and TiO_2/GQDs (2.2 μmol/h) photocatalysts published by Min et al. [6]. The above results show that the combination of pure TiO_2 and GQDs is an effective means to improve the activity of photocatalytic H_2 production. Due to the strong coupling between TiO_2 caterpillar and GQDs, the electron-hole pairs at the interface between GQDs and TiO_2 are effectively separated through the C–O–Ti bonds, resulting in high photocatalytic H_2 evolution activity. In addition, there is hot electron injection from GQDs to TiO_2 caterpillar, which is also conducive to photocatalytic performance [56].

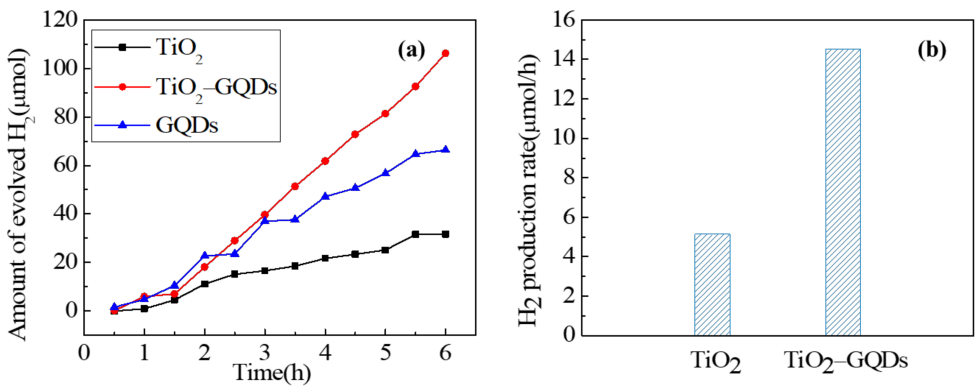

Figure 7. (**a**) Amount of photocatalytic H_2 production, and (**b**) average photocatalytic H_2 production rate for different samples under simulated solar light irradiation.

3.7. Analysis of Photocatalytic Hydrogen Generation Mechanism

Based on the above results, a possible interfacial charge transfer mechanism of photocatalytic hydrogen production for TiO_2-GQDs caterpillar hybrid is illustrated in Figure 8a. The TiO_2-GQDs heterojunction forms a type-II (staggered gap) band alignment, which is more thermodynamically favorable. First, since the incorporation of GQDs reduces the band gap and the synergistic effect between TiO_2 caterpillar and GQDs, both UV and visible region of incident light can be utilized simultaneously in the TiO_2-GQDs hybrid to produce electron-hole pairs. TiO_2 can absorb the UV part of the incident light, while GQDs absorb visible light. Second, the attractive heterostructure can lead to charge separation at the interface, where GQDs and TiO_2 act as donor and acceptor, respectively. The possible C–O–Ti bond was formed by rearranging epoxy functional groups in GQDs and oxygen vacancies in TiO_2 caterpillar, which further enhanced the interfacial electron transfer from GQDs to TiO_2. A schematic model for the C–O–Ti bond in hybrid is presented in Figure 8b. Another key factor is the existence of hot electron injection from GQDs to TiO_2 caterpillar due to the strong interaction between them. Finally, once the charges are separated, the CB electrons of TiO_2 which transferred from GQDs and generated by TiO_2 will migrate to the surface and react with water molecules to produce H_2. In addition, the highly ordered 3D TiO_2 caterpillar nanoarchitecture can shorten the lateral diffusion pathways of charge carriers to the surface due to its large specific surface area and promote better dispersion of GQDs to extend the number of active sites. As a result, the introduction of GQDs not only extends the visible light response region but also increases the charge separation rate in

order to improve the photocatalytic hydrogen production capacity of TiO_2 caterpillar. The entire photocatalytic reaction process can be described by the following equations [45]:

$$photocatalyst + hv \rightarrow e^- + h^+, \quad (3)$$

$$h^+ + H_2O \rightarrow \cdot OH + H^+, \quad (4)$$

$$CH_3OH + \cdot OH \rightarrow \cdot CH_2OH + H_2O, \quad (5)$$

$$\cdot CH_2OH \rightarrow HCHO + H^+ + e^-, \quad (6)$$

$$2H_2O + 2e^- \rightarrow H_2 + 2OH^-, \quad (7)$$

$$\text{overall reaction}: \quad CH_3OH \rightarrow HCHO + H_2, \quad (8)$$

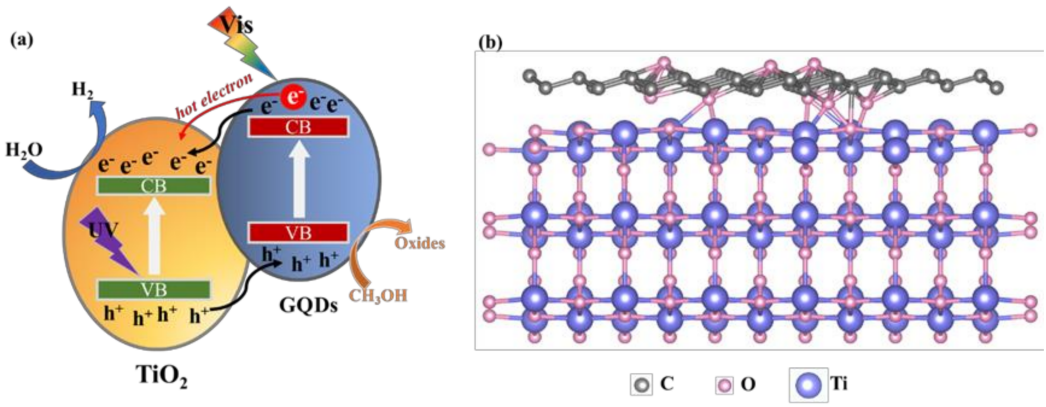

Figure 8. (**a**) Schematic of interfacial carrier transfer mechanism of photocatalytic hydrogen production for TiO_2-GQDs caterpillar hybrid. (**b**) Schematic model for the C–O–Ti bond.

4. Conclusions

In summary, the designed TiO_2-GQDs caterpillar hybrid was employed to study its photocatalytic water reduction for hydrogen production. It is proposed that ultrasound can induce the formation of oxygen vacancies in TiO_2 caterpillars, and the rearrangement of in-plane epoxy functional groups in GQDs, such that they can form hybrids through the possible C–O–Ti bonds. The addition of GQDs to TiO_2 caterpillar results in a stronger visible light absorption capability and the well-matched band-structure of the TiO_2-GQDs hybrid theoretically satisfies the water photo-splitting for hydrogen production. The hydrogen evolution rate of TiO_2-GQDs hybrid can reach 18.3 μmol/h, which is over 3.5 times that of pure TiO_2. The enhanced photocatalytic activity of hybrid may be attributed to the unique morphology of caterpillar nanoarchitecture and rapid interfacial electron transfer from GQDs to TiO_2 via the C–O–Ti bonds. This work will contribute to the development of low-cost and high-efficiency photocatalysts with unique morphology and provide ideas for more fields of research.

Author Contributions: Conceptualization, J.M. and L.C.; methodology, Y.G. and J.M.; validation, C.S., Z.L., and H.Y.; investigation, Y.G.; data curation, C.S.; writing—original draft preparation, J.M. and Y.G.; writing—review and editing, L.C. and M.L.; supervision, M.L. All authors have read and agreed to the published version of the manuscript.

Funding: This research was funded partially by Natural Science Foundation of Beijing Municipality (L172036), Joint Funds of the Equipment Pre-Research and Ministry of Education (6141A020225), Par-Eu Scholars Program, Science and Technology Beijing 100 Leading Talent Training Project, and the Fundamental Research Funds for the Central Universities (2020MS028, 2020FR002, 2020MS023), the NCEPU "Double First-Class" Program.

Institutional Review Board Statement: Not applicable.

Informed Consent Statement: Not applicable.

Data Availability Statement: The data presented in this study are available on request from the corresponding author.

Conflicts of Interest: The authors declare no conflict of interest. The funders had no role in the design of the study; in the collection, analyses, or interpretation of data; in the writing of the manuscript; or in the decision to publish the results.

References

1. Chu, S.; Cui, Y.; Liu, N. The path towards sustainable energy. *Nat. Mater.* **2017**, *16*, 16–22. [CrossRef] [PubMed]
2. Qiu, B.; Zhu, Q.; Du, M.; Fan, L.; Xing, M.; Zhang, J. Efficient Solar Light Harvesting CdS/Co_9S_8 Hollow Cubes for Z-Scheme Photocatalytic Water Splitting. *Angew. Chem. Int. Ed.* **2017**, *56*, 2684–2688. [CrossRef]
3. Yuan, Y.-J.; Tu, J.-R.; Ye, Z.-J.; Chen, D.-Q.; Hu, B.; Huang, Y.-W.; Chen, T.-T.; Cao, D.-P.; Yu, Z.-T.; Zou, Z.-G. MoS_2-graphene/$ZnIn_2S_4$ hierarchical microarchitectures with an electron transport bridge between light-harvesting semiconductor and cocatalyst: A highly efficient photocatalyst for solar hydrogen generation. *Appl. Catal. B* **2016**, *188*, 13–22. [CrossRef]
4. Zhang, Q.; Wang, H.; Chen, S.; Su, Y.; Quan, X. Three-dimensional TiO_2 nanotube arrays combined with g-C_3N_4 quantum dots for visible light-driven photocatalytic hydrogen production. *RSC Adv.* **2017**, *7*, 13223–13227. [CrossRef]
5. Jangid, N.K.; Jadoun, S.; Yadav, A.; Srivastava, M.; Kaur, N. Polyaniline-TiO_2-based photocatalysts for dyes degradation. *Polym. Bull.* **2021**, *78*, 4743–4777. [CrossRef]
6. Min, S.; Hou, J.; Lei, Y.; Ma, X.; Lu, G. Facile one-step hydrothermal synthesis toward strongly coupled TiO_2/graphene quantum dots photocatalysts for efficient hydrogen evolution. *Appl. Surf. Sci.* **2017**, *396*, 1375–1382. [CrossRef]
7. Peiris, S.; de Silva, H.B.; Ranasinghe, K.N.; Bandara, S.V.; Perera, I.R. Recent development and future prospects of TiO_2 photocatalysis. *J. Chin. Chem. Soc.* **2021**, *68*, 738–769. [CrossRef]
8. Wang, C.; Zhang, X. Anatase/Bronze TiO_2 Heterojunction: Enhanced Photocatalysis and Prospect in Photothermal Catalysis. *Chem. Res. Chin. Univ.* **2020**, *36*, 992–999. [CrossRef]
9. Seo, D.-B.; Bae, S.-S.; Kim, E.-T. Efficient Visible-Light Photocatalysis of TiO_2-delta Nanobelts Utilizing Self-Induced Defects and Carbon Doping. *Nanomaterials* **2021**, *11*, 1377. [CrossRef]
10. Li, K.; Chen, R.; Li, S.-L.; Xie, S.-L.; Dong, L.-Z.; Kang, Z.-H.; Bao, J.-C.; Lan, Y.-Q. Engineering $Zn_{1-x}Cd_xS$/CdS Heterostructures with Enhanced Photocatalytic Activity. *ACS Appl. Mater. Interfaces* **2016**, *8*, 14535–14541. [CrossRef]
11. Lei, Y.; Yang, C.; Hou, J.; Wang, F.; Min, S.; Ma, X.; Jin, Z.; Xu, J.; Lu, G.; Huang, K.-W. Strongly coupled CdS/graphene quantum dots nanohybrids for highly efficient photocatalytic hydrogen evolution: Unraveling the essential roles of graphene quantum dots. *Appl. Catal. B* **2017**, *216*, 59–69. [CrossRef]
12. Tian, X.-T.; Yin, X.-B. Carbon Dots, Unconventional Preparation Strategies, and Applications Beyond Photoluminescence. *Small* **2019**, *15*, 1901803. [CrossRef] [PubMed]
13. Tu, X.; Wang, Q.; Zhang, F.; Lan, F.; Liu, H.; Li, R. CO_2-triggered reversible phase transfer of graphene quantum dots for visible light-promoted amine oxidation. *Nanoscale* **2020**, *12*, 4410–4417. [CrossRef] [PubMed]
14. Mueller, M.L.; Yan, X.; Dragnea, B.; Li, L.-s. Slow Hot-Carrier Relaxation in Colloidal Graphene Quantum Dots. *Nano Lett.* **2011**, *11*, 56–60. [CrossRef]
15. Liu, X.; Jian, X.; Yang, H.; Song, X.; Liang, Z. A photocatalytic graphene quantum dots-Cu_2O/bipolar membrane as a separator for water splitting. *New J. Chem.* **2016**, *40*, 3075–3079. [CrossRef]
16. Ryu, J.; Lee, J.W.; Yu, H.; Yun, J.; Lee, K.; Lee, J.; Hwang, D.; Kang, J.; Kim, S.K.; Jang, J. Size effects of a graphene quantum dot modified-blocking TiO_2 layer for efficient planar perovskite solar cells (vol 5, pg 18276, 2017). *J. Mater. Chem. A* **2017**, *5*, 18276. [CrossRef]
17. Chen, Y.; Bai, X. A Review on Quantum Dots Modified g-C_3N_4-Based Photocatalysts with Improved Photocatalytic Activity. *Catalysts.* **2020**, *10*, 142. [CrossRef]
18. Wei, D.; Tang, W.; Gan, Y.; Xu, X. Graphene quantum dot-sensitized Zn-MOFs for efficient visible-light-driven carbon dioxide reduction. *Catal. Sci. Technol.* **2020**, *10*, 5666–5676. [CrossRef]
19. Biswas, A.; Salunke, G.; Khandelwal, P.; Das, R.; Poddar, P. Surface disordered rutile TiO_2-graphene quantum dot hybrids: A new multifunctional material with superior photocatalytic and biofilm eradication properties. *New J. Chem.* **2017**, *41*, 2642–2657. [CrossRef]
20. Safardoust-Hojaghan, H.; Salavati-Niasari, M. Degradation of methylene blue as a pollutant with N-doped graphene quantum dot/titanium dioxide nanocomposite. *J. Clean. Prod.* **2017**, *148*, 31–36. [CrossRef]
21. Liu, H.; Chen, Z.; Zhang, L.; Zhu, D.; Zhang, Q.; Luo, Y.; Shao, X. Graphene Grown on Anatase-TiO_2 Nanosheets: Enhanced Photocatalytic Activity on Basis of a Well-Controlled Interface. *J. Phys. Chem. C* **2018**, *122*, 6388–6396. [CrossRef]
22. Peng, J.; Gao, W.; Gupta, B.K.; Liu, Z.; Romero-Aburto, R.; Ge, L.; Song, L.; Alemany, L.B.; Zhan, X.; Gao, G.; et al. Graphene Quantum Dots Derived from Carbon Fibers. *Nano Lett.* **2012**, *12*, 844–849. [CrossRef] [PubMed]
23. Li, X.; Wu, G.; Liu, X.; Li, W.; Li, M. Orderly integration of porous TiO_2(B) nanosheets into bunchy hierarchical structure for high-rate and ultralong-lifespan lithium-ion batteries. *Nano Energy* **2017**, *31*, 1–8. [CrossRef]
24. Tian, H.; Shen, K.; Hu, X.; Qiao, L.; Zheng, W. N, S co-doped graphene quantum dots-graphene-TiO_2 nanotubes composite with enhanced photocatalytic activity. *J. Alloy. Compd.* **2017**, *691*, 369–377. [CrossRef]

25. Georgakilas, V.; Perman, J.A.; Tucek, J.; Zboril, R. Broad Family of Carbon Nanoallotropes: Classification, Chemistry, and Applications of Fullerenes, Carbon Dots, Nanotubes, Graphene, Nanodiamonds, and Combined Superstructures. *Chem. Rev.* **2015**, *115*, 4744–4822. [CrossRef] [PubMed]
26. Chinnusamy, S.; Kaur, R.; Bokare, A.; Erogbogbo, F. Incorporation of graphene quantum dots to enhance photocatalytic properties of anatase TiO_2. *MRS Commun.* **2018**, *8*, 137–144. [CrossRef]
27. Ebrahimi, M.; Samadi, M.; Yousefzadeh, S.; Soltani, M.; Rahimi, A.; Chou, T.-c.; Chen, L.-C.; Chen, K.-H.; Moshfegh, A.Z. Improved Solar-Driven Photocatalytic Activity of Hybrid Graphene Quantum Dots/ZnO Nanowires: A Direct Z-Scheme Mechanism. *ACS Sustain. Chem. Eng.* **2017**, *5*, 367–375. [CrossRef]
28. Gao, Y.; Hou, F.; Hu, S.; Wu, B.; Wang, Y.; Zhang, H.; Jiang, B.; Fu, H. Graphene Quantum-Dot-Modified Hexagonal Tubular Carbon Nitride for Visible-Light Photocatalytic Hydrogen Evolution. *Chemcatchem* **2018**, *10*, 1330–1335. [CrossRef]
29. Yang, C.-H.; Ma, Z.-Q. Raman spectral analysis of TiO_2 thin films doped with rare-earth samarium. *Appl. Opt.* **2012**, *51*, 5438–5441. [CrossRef]
30. Wang, C.-X.; Chen, Y.; Fan, Y.-Z.; Zhang, Y.-W.; Liang, Q.-Y.; Wu, Y.-D.; Li, D.-M.; Jia, J.-F.; Xue, Q.-K.; Zhao, Z.-Q.; et al. Study on the mechanism of visible absorption enhancement for N^+ implanted TiO_2 by Raman spectroscopy. *Surf. Rev. Lett.* **2011**, *18*, 135–140. [CrossRef]
31. Thang, P.N.; Hung, L.X.; Thuan, D.N.; Yen, N.H.; Hien, N.T.T.; Hanh, V.T.H.; Khang, N.C.; Laverdant, J.; Nga, P.T. Temperature-dependent Raman investigation and photoluminescence of graphene quantum dots with and without nitrogen-doping. *J. Mater. Sci.* **2021**, *56*, 4979–4990. [CrossRef]
32. Wu, X.; Zhao, J.; Guo, S.; Wang, L.; Shi, W.; Huang, H.; Liu, Y.; Kang, Z. Carbon dot and $BiVO_4$ quantum dot composites for overall water splitting via a two-electron pathway. *Nanoscale* **2016**, *8*, 17314–17321. [CrossRef] [PubMed]
33. Giannakoudakis, D.A.; Farahmand, N.; Lomot, D.; Sobczak, K.; Bandosz, T.J.; Colmenares, J.C. Ultrasound-activated TiO_2/GO-based bifunctional photoreactive adsorbents for detoxi fication of chemical warfare agent surrogate vapors. *Chem. Eng. J.* **2020**, *395*, 125099. [CrossRef]
34. Umrao, S.; Abraham, S.; Theil, F.; Pandey, S.; Ciobota, V.; Shukla, P.K.; Rupp, C.J.; Chakraborty, S.; Ahuja, R.; Popp, J.; et al. A possible mechanism for the emergence of an additional band gap due to a Ti–O–C bond in the TiO_2-graphene hybrid system for enhanced photodegradation of methylene blue under visible light. *RSC Adv.* **2014**, *4*, 59890–59901. [CrossRef]
35. Xing, M.; Shen, F.; Qiu, B.; Zhang, J. Highly-dispersed Boron-doped Graphene Nanosheets Loaded with TiO_2 Nanoparticles for Enhancing CO_2 Photoreduction. *Sci. Rep.* **2014**, *4*, 6341. [CrossRef]
36. Zhang, J.; Dong, Z.; Wang, X.; Zhao, X.; Tu, J.; Su, Q.; Du, G. Sulfur nanocrystals anchored graphene composite with highly improved electrochemical performance for lithium-sulfur batteries. *J. Power Sources* **2014**, *270*, 1–8. [CrossRef]
37. Yan, X.; Li, Y.; Li, M.; Jin, Y.; Du, F.; Chen, G.; Wei, Y. Ultrafast lithium storage in TiO_2-bronze nanowires/N-doped graphene nanocomposites. *J. Mater. Chem. A* **2015**, *3*, 4180–4187. [CrossRef]
38. Yu, S.; Zhong, Y.-Q.; Yu, B.-Q.; Cai, S.-Y.; Wu, L.-Z.; Zhou, Y. Graphene quantum dots to enhance the photocatalytic hydrogen evolution efficiency of anatase TiO_2 with exposed {001} facet. *PCCP* **2016**, *18*, 20338–20344. [CrossRef]
39. Choi, H.C.; Jung, Y.M.; Kim, S.B. Size effects in the Raman spectra of TiO_2 nanoparticles. *Vib. Spectrosc* **2005**, *37*, 33–38. [CrossRef]
40. Santara, B.; Giri, P.K.; Imakita, K.; Fujii, M. Evidence of oxygen vacancy induced room temperature ferromagnetism in solvothermally synthesized undoped TiO_2 nanoribbons. *Nanoscale* **2013**, *5*, 5476–5488. [CrossRef]
41. Bahruji, H.; Bowker, M.; Davies, P.R. Influence of TiO_2 structural properties on photocatalytic hydrogen gas production. *J. Chem. Sci.* **2019**, *131*, 33. [CrossRef]
42. Rajender, G.; Kumar, J.; Giri, P.K. Interfacial charge transfer in oxygen deficient TiO_2-graphene quantum dot hybrid and its influence on the enhanced visible light photocatalysis. *Appl. Catal. B* **2018**, *224*, 960–972. [CrossRef]
43. Karthik, P.; Vinesh, V.; Shaheer, A.R.M.; Neppolian, B. Self-doping of Ti^{3+} in TiO_2 through incomplete hydrolysis of titanium (IV) isopropoxide: An efficient visible light sonophotocatalyst for organic pollutants degradation. *Appl. Catal. A* **2019**, *585*, 117208. [CrossRef]
44. Abdullah, S.A.; Sandan, M.Z.; Nayan, N.; Embong, Z.; Hak, C.R.C.; Adriyanto, F. Neutron beam interaction with rutile TiO_2 single crystal (111): Raman and XPS study on Ti3+-oxygen vacancy formation. *Mater. Lett.* **2020**, *263*, 127143. [CrossRef]
45. Xie, H.; Hou, C.; Wang, H.; Zhang, Q.; Li, Y. S, N Co-Doped Graphene Quantum Dot/TiO_2 Composites for Efficient Photocatalytic Hydrogen Generation. *Nanoscale Res. Lett.* **2017**, *12*, 400. [CrossRef]
46. Shafaee, M.; Goharshadi, E.K.; Mashreghi, M.; Sadeghinia, M. TiO_2 nanoparticles and TiO_2@graphene quantum dots nancomposites as effective visible/solar light photocatalysts. *J. Photochem. Photobiol. A* **2018**, *357*, 90–102. [CrossRef]
47. Makula, P.; Pacia, M.; Macyk, W. How To Correctly Determine the Band Gap Energy of Modified Semiconductor Photocatalysts Based on UV-Vis Spectra. *J. Phys. Chem. Lett.* **2018**, *9*, 6814–6817. [CrossRef]
48. Liu, Y.; Zhang, H.; Ke, J.; Zhang, J.; Tian, W.; Xu, X.; Duan, X.; Sun, H.; Tade, M.O.; Wang, S. 0D (MoS_2)/2D (g-C_3N_4) heterojunctions in Z-scheme for enhanced photocatalytic and electrochemical hydrogen evolution. *Appl. Catal. B* **2018**, *228*, 64–74. [CrossRef]
49. Wang, Y.; Liu, X.; Liu, J.; Han, B.; Hu, X.; Yang, F.; Xu, Z.; Li, Y.; Jia, S.; Li, Z.; et al. Carbon Quantum Dot Implanted Graphite Carbon Nitride Nanotubes: Excellent Charge Separation and Enhanced Photocatalytic Hydrogen Evolution. *Angew. Chem. Int. Ed.* **2018**, *57*, 5765–5771. [CrossRef]

50. Xia, Y.; Li, Q.; Lv, K.; Tang, D.; Li, M. Superiority of graphene over carbon analogs for enhanced photocatalytic H_2 production activity of $ZnIn_2S_4$. *Appl. Catal. B* **2017**, *206*, 344–352. [CrossRef]
51. He, R.; Liu, H.; Liu, H.; Xu, D.; Zhang, L. S-scheme photocatalyst Bi_2O_3/TiO_2 nanofiber with improved photocatalytic performance. *J. Mater. Sci. Technol.* **2020**, *52*, 145–151.
52. Yang, P.; Zhao, J.; Wang, J.; Cao, B.; Li, L.; Zhu, Z. Construction of Z-scheme carbon nanodots/WO_3 with highly enhanced photocatalytic hydrogen production. *J. Mater. Chem. A* **2015**, *3*, 8256–8259. [CrossRef]
53. Chang, D.W.; Baek, J.-B. Nitrogen-Doped Graphene for Photocatalytic Hydrogen Generation. *Chem Asian J* **2016**, *11*, 1125–1137. [CrossRef] [PubMed]
54. Kudo, A.; Miseki, Y. Heterogeneous photocatalyst materials for water splitting. *Chem. Soc. Rev.* **2009**, *38*, 253–278. [CrossRef] [PubMed]
55. Yu, H.; Zhao, Y.; Zhou, C.; Shang, L.; Peng, Y.; Cao, Y.; Wu, L.-Z.; Tung, C.-H.; Zhang, T. Carbon quantum dots/TiO_2 composites for efficient photocatalytic hydrogen evolution. *J. Mater. Chem. A* **2014**, *2*, 3344–3351. [CrossRef]
56. Williams, K.J.; Nelson, C.A.; Yan, X.; Li, L.-S.; Zhu, X. Hot Electron Injection from Graphene Quantum Dots to TiO_2. *ACS Nano* **2013**, *7*, 1388–1394. [CrossRef] [PubMed]